Zaman *et al. Energy Mater.* **2025**, *5*, 500028
DOI: 10.20517/energymater.2024.133

Energy Materials

Article

Open Access

Check for updates

Formation of a stable LiF-rich SEI layer on molybdenum-based MXene electrodes for enhanced lithium metal batteries

Shakir Zaman[1], Mugilan Narayanasamy[1], Shabbir Madad Naqvi[1], Tufail Hassan[1], Aamir Iqbal[1], Ujala Zafar[1], Noushad Hussain[1], Seunghwan Jeong[1], Soo Yeong Cho[1], Sungmin Jung[1], Chong Min Koo[1,2,*]

[1]School of Advanced Materials Science and Engineering, Sungkyunkwan University, Gyeonggi-do 16419, Republic of Korea.
[2]School of Chemical Engineering, Sungkyunkwan University, Gyeonggi-do 16419, Republic of Korea.

***Correspondence to:** Dr. Chong Min Koo, School of Advanced Materials Science and Engineering, Sungkyunkwan University, Seobu-ro 2066, Jangan-gu, Suwon-si, Gyeonggi-do 16419, Republic of Korea. E-mail:chongminkoo@skku.edu

How to cite this article: Zaman, S.; Narayanasamy, M.; Naqvi, S. M.; Hassan, T.; Iqbal, A.; Zafar, U.; Hussain, N.; Jeong, S.; Cho, S. Y.; Jung, S.; Koo, C. M. Formation of a stable LiF-rich SEI layer on molybdenum-based MXene electrodes for enhanced lithium metal batteries. *Energy Mater.* **2025**, *5*, 500028. https://dx.doi.org/10.20517/energymater.2024.133

Received: 23 Aug 2024 **First Decision:** 21 Sep 2024 **Revised:** 11 Oct 2024 **Accepted:** 23 Oct 2024 **Published:** 17 Jan 2025

Academic Editor: Bin Wang **Copy Editor:** Fangling Lan **Production Editor:** Fangling Lan

Abstract

Lithium metal batteries are considered highly promising candidates for the next-generation high-energy storage system. However, the growth of lithium dendrites significantly hinders their advance, particularly under high current densities, due to the formation of unstable solid electrolyte interphase (SEI) layers. In this study, we demonstrate that molybdenum-based MXenes, including Mo_2CT_x, $Mo_2TiC_2T_x$, and $Mo_2Ti_2C_3T_x$, form more stable LiF/Li_2CO_3 SEI layers during lithium plating, compared to the conventional Cu electrode. Among these, the bimetallic $Mo_2Ti_2C_3T_x$ MXene, with its higher fluorine terminations, produces the most stable LiF-rich SEI layer. The formation of this stable inorganic SEI layer significantly reduces the nucleation overpotential for lithium deposition, promotes uniform Li deposition, and suppresses dendrite growth. Consequently, the $Mo_2Ti_2C_3T_x$ substrate achieved prolonged cycling stability of approximately 544 cycles with coulombic efficiency of ~99.79% at high current density of 3 mA cm^{-2} and capacity of 1 mAh cm^{-2}. In full cells, the $Mo_2Ti_2C_3T_x$ anode, paired with an NCM622 cathode, maintained capacity retention of 70% over 100 cycles with high cathode loading of 10 mg cm^{-2}. Our approach highlights the potential of Mo-based MXenes to improve the performance of lithium metal batteries, making them promising candidates for the next-generation energy storage system.

Keywords: Lithium metal battery, molybdenum MXenes, SEI layer, lithium dendrite

INTRODUCTION

Lithium metal batteries (LMBs) have garnered significant attention as next-generation power sources due to the high theoretical capacity of lithium metal anodes (3,860 mAh g^{-1}), compared to that of the conventional graphite anodes (372 mAh g^{-1})[1-3]. However, the practical application of LMBs is currently hindered by their poor cycle life, which results from the uncontrollable growth of lithium dendrites and the collapse of the solid electrolyte interface (SEI) layer on the anode, particularly at high current densities. These issues lead to significant volume change, fast electrolyte consumption, low coulombic efficiency (CE), rapid capacity decay, and ultimately, deteriorated cycling performance[4,5].

The primary roles of the SEI layer are to protect the electrode from unwanted side reactions with lithium metal and to minimize the capacity loss during cycling[6]. The formation of a stable fluorine-rich inorganic SEI layer, such as lithium fluoride (LiF), is imperative for the uniform deposition of Li^+ ions at the Li-substrate interface due to its notable characteristics, which include fast ion diffusion, low diffusion energy, and elevated surface energy[7-9].

The F-rich inorganic SEIs can be strategically developed through electrolyte engineering[10,11] and the surface modification of electrodes[12,13]. Despite progress, electrolyte engineering approaches, such as using highly concentrated F-containing salt compositions and fluorinated solvents, face significant challenges for practical implementation. The high salt concentrations required for these electrolytes are difficult to incorporate into commercial battery systems, and replacing conventional solvents with fluorinated ones significantly increases electrolyte viscosity and battery costs[14]. Alternatively, modifying the electrode surface with lithiophilic coatings has been considered the most promising method to form stable F-rich SEI layers[15,16].

MXenes, which are two-dimensional transition metal carbides, nitrides, and carbonitrides, have emerged as potential anode substrates for LMBs, due to the electrochemical activity of their abundant surface termination groups, such as -OH, -O, and -F[17,18]. These negatively charged surface groups make MXene lithiophilic, providing numerous lithium nucleation sites. This characteristic reduces the overpotential during lithium deposition, promotes uniform lithium growth, and suppresses dendrite formation.

To date, titanium (Ti)-based MXenes, such as $Ti_3C_2T_x$, have been extensively utilized in LMBs for multiple purposes, including serving as lithiophilic hosts to stabilize the SEI[19], designing 3D MXene-based substrates to mitigate volume changes[20], creating an artificial SEI layer for electrode/electrolyte interface stability[21], and acting as additives to improve the ionic conductivity of solid electrolytes[22]. However, further investigation is urgently required into SEI layers on MXenes that facilitate lithium plating/stripping at higher current densities on commercial Cu substrates. Additionally, designing a suitable MXene anode structure that can maintain a stable SEI layer and enable repeated cycling under high-power operating conditions is critical for next-generation high-energy-density battery applications. Furthermore, despite the development of over 50 types of MXenes since their discovery in 2011, battery research has predominantly concentrated on a few monometallic MXenes, such as $Ti_3C_2T_x$, Nb_2CT_x, and V_2CT_x, due to the low yield of the synthesized MXenes, and their environmental stability[23].

Herein, we report that three types of Mo-based MXenes - monometallic Mo_2CT_x and bimetallic $Mo_2TiC_2T_x$ and $Mo_2Ti_2C_3T_x$ - form more stable inorganic LiF/Li_2CO_3 SEI layers during lithium plating, compared to the conventional Cu electrode. Notably, the bimetallic $Mo_2Ti_2C_3T_x$ MXene forms the most stable LiF-rich SEI layer, which is attributed to its abundant F-terminations on the surface, which significantly suppresses dendrite growth. Consequently, the $Mo_2Ti_2C_3T_x$ substrate achieves prolonged cycling stability of

approximately 544 cycles with CE of ~99.79% at high current density of 3 mA cm^{-2} and capacity of 1 mAh cm^{-2}.

EXPERIMENTAL

Materials

Mo_2AlC, Mo_2TiAlC_2, and $Mo_2Ti_2AlC_3$ MAX-phase powders with average particle sizes of 40 μm were purchased from Jilin 11 Technology (China). Hydrogen fluoride (HF; 48 wt.% in H_2O), tetramethylammonium hydroxide (TMAOH; 25 wt.% in H_2O), poly(vinylidene fluoride) (PVDF), and Super P carbon were purchased from Sigma-Aldrich. N-methyl-2-pyrrolidone (NMP; 99.5%) was procured from Daejung Chemicals. Commercial NCM622 powders were purchased from MTI-Korea (Republic of Korea). Polypropylene (PP) separator (Celgard 3501) was acquired from MTI-Korea (Republic of Korea). All chemicals were used as received.

Synthesis of the Mo_2CT_x, $Mo_2TiC_2T_x$, and $Mo_2Ti_2C_3T_x$ MXenes

The Mo_2CT_x, $Mo_2TiC_2T_x$, and $Mo_2Ti_2C_3T_x$ MXenes were synthesized by selectively removing Ga from Mo_2Ga_2C and Al from Mo_2TiAlC_2 and $Mo_2Ti_2AlC_3$, using aqueous HF etchant[24,25]. Specifically, an aqueous HF solution (20 mL; 48%) was separately mixed with the selected MAX powders (1 g) in PP bottles at 55 °C in a gradual manner. Etching reactions proceeded for 168, 48, and 96 h for the Mo_2Ga_2C, Mo_2TiAlC_2, and $Mo_2Ti_2AlC_3$, respectively. After the reaction, the etched solutions were washed with deionized water, and repeatedly centrifuged at 3,500 rpm for 10 min, until the supernatant reached a pH of (5-6). The residual powders were slightly dried, and dispersed to be delaminated overnight in a TMAOH solution (10 mL, 10 wt.%). The products were washed three to four times via centrifugation at 10,000 rpm for 30 min to remove as much residual TMAOH as possible, until the pH reached (8-9). The MXenes supernatants were centrifuged at 3,500 rpm for 30 min to obtain delaminated MXene flakes with yield of Mo_2CT_x, $Mo_2TiC_2T_x$, and $Mo_2Ti_2C_3T_x$ of 10, 25, and 30%, respectively.

Preparation of the Mo_2CT_x, $Mo_2TiC_2T_x$, and $Mo_2Ti_2C_3T_x$ electrodes

To prepare the MXene electrodes coated on Cu substrates, Mo_2CT_x, $Mo_2TiC_2T_x$, and $Mo_2Ti_2C_3T_x$ freeze-dried powders were mixed with poly-vinylidene fluoride and Super P carbon in a mass ratio of 8:1:1 using N-methyl pyrrolidone (NMP) solvent to make a homogeneous slurry. The slurry was coated on the Cu foil using a doctor blade, and dried in a vacuum oven at 80 °C for 8 h to effectively eliminate any residual solvent content. The thickness of Cu foil is 17 μm. The average thickness of the MXene coating layer was approximately 3 μm.

Cell assembly and electrochemical measurements

All electrochemical tests were carried out using 2032-type coin cells that were assembled in an Ar-filled glove box. Half-cell measurements were carried out using a 14 mm diameter MXenes-coated current collector, with Li foil as counter and reference electrode (12 mm in diameter). Celgard 3501 PP membrane was used as a separator in this study. The electrolyte for half-cell was 1 M lithium bis(trifluoromethane sulfonyl) imide (LiTFSI) in 1,3-dioxolane/1,2-dimethoxyethane (DOL/DME;1:1, v/v) with 5 wt.% $LiNO_3$. For full cell measurements, the NCM622 electrode sheets were used as the cathode, and the Li pre-deposited MXene-coated Cu as the anode. The electrolyte for full cells was 1M $LiPF_6$ in ethyl carbonate/dimethyl carbonate (EC/DMC). The electrolyte quantity was fixed at 75 μL. Battery cycling tests were conducted using a WonATech battery cycler. Electrochemical impedance spectroscopy (EIS) was performed using a Bio-Logic VMP3 impedance analyzer at room temperature.

Materials characterization

The X-ray photoelectron spectroscopy (XPS, ESCALAB250 system) analysis was carried out using an Al-anode source. X-ray diffractometry (XRD) measurements (Smartlab, Rigaku) were performed under 2 range of 3°-80° using a Cu-kα radiation source. Field emission scanning electron microscopy (FE-SEM) images were captured using a JSM-7600F instrument. Transmission electron microscopy (TEM) images were taken using the JEM-ARM200CF apparatus.

RESULTS AND DISCUSSION

Preparation of the Mo-based MXene anode substrates

Three types of Mo-based MXenes of Mo_2CT_x, $Mo_2TiC_2T_x$, and $Mo_2Ti_2C_3T_x$ were synthesized by selectively etching Al or Ga from their corresponding MAX phases (Mo_2Ga_2C, Mo_2TiAlC_2, and $Mo_2Ti_2AlC_3$, respectively), using HF etching solution [Figure 1A]. Detailed synthesis procedures are provided in the Section "EXPERIMENTAL", following previously reported methods. The XRD patterns of the three Mo-based MXenes [Figure 1B] clearly demonstrate the successful etching synthesis, which is evidenced by the shift of the 002 peak toward a lower angle, corresponding to an increase in the interlayer spacing between MXene layers. Additionally, the disappearance of the peak at around 39° suggests the successful etching of the Al or Ga element[26-28]. The TEM images of the $Mo_2Ti_2C_3T_x$ [Figure 1C], $Mo_2TiC_2T_x$, and Mo_2CT_x [Supplementary Figure 1], coupled with selected area electron diffraction (SAED) patterns, revealed that the MXenes were well delaminated to provide single-sheet morphology. MXenes had an average diameter of 1-2 μm [Supplementary Figure 2]. The Mo-based MXene films prepared by vacuum-assisted filtration of the MXene aqueous dispersions showed black and dark-gray colors in the optical imagery [Supplementary Figure 3].

The surface chemistry and stoichiometry of the Mo_2CT_x, $Mo_2TiC_2T_x$, and $Mo_2Ti_2C_3T_x$ films are determined by XPS [Figure 1D and E, Supplementary Figures 4-6]. For the Mo 3d spectra [Figure 1E], the Mo_2CT_x showed peaks at binding energies (BEs) of 231.98, 230.52, and 233.73 eV, which are attributed to Mo-C, Mo^{4+}, and Mo^{5+} species, respectively. The $Mo_2TiC_2T_x$ exhibited contributions from the Mo^{5+} and Mo^{6+} at BEs of 230.82 and 235.78 eV, respectively. The $Mo_2Ti_2C_3T_x$ exhibited peaks at 229.57, 230.9, and 234.14 eV, corresponding to the Mo-C and/or Mo-C-Ti/T_x, Mo^{5+}, and Mo^{6+} species, respectively. The deconvoluted C 1s, F 1s, O 1s, and Ti 2p XPS profiles of the Mo_2CT_x and $Mo_2TiC_2T_x$ MXenes are also provided [Supplementary Figures 4 and 5]. These Mo 3d, Ti 2p, C 1s, F 1s, and O 1s spectra for the Mo_2CT_x, $Mo_2TiC_2T_x$, and $Mo_2Ti_2C_3T_x$ were consistent with previously reported data[29], indicating the successful synthesis of the Mo-based MXenes without impurities or surface oxidation. Notably, the Mo_2CT_x, $Mo_2TiC_2T_x$, and $Mo_2Ti_2C_3T_x$ revealed different surface chemistries. Among them, the bimetallic $Mo_2Ti_2C_3T_x$ exhibited the highest -F terminations (5.2%) in a comparative XPS study [Figure 1D and F], which may play an important role in the formation of LiF-rich SEI. The elemental concentrations for Mo_2CT_x, $Mo_2TiC_2T_x$, and $Mo_2Ti_2C_3T_x$ films are provided in [Supplementary Table 1].

The fabrication of the Mo_2CT_x, $Mo_2TiC_2T_x$, and $Mo_2Ti_2C_3T_x$ electrodes involves preparing a slurry by mixing freeze-dried MXenes powder, PVDF, and super P conducting agent in a weight ratio of 8:1:1 in NMP, then casting the slurry onto a Cu substrate (Details are provided in the Section "EXPERIMENTAL"). The resulting MXene electrodes coated on the Cu substrate exhibited a smooth surface with a coating thickness of approximately 3 μm, as shown in the digital photograph and cross-section scanning electron microscopy (SEM) image [Figure 1G and Supplementary Figure 7]. The uniformity of MXene coating is further confirmed by the energy dispersive spectroscopy (EDS) mapping in [Supplementary Figure 8]. These Mo-based MXene electrodes were then utilized for further electrochemical examinations to investigate their SEI formation, lithium deposition, and dendrite formation behavior in LMBs.

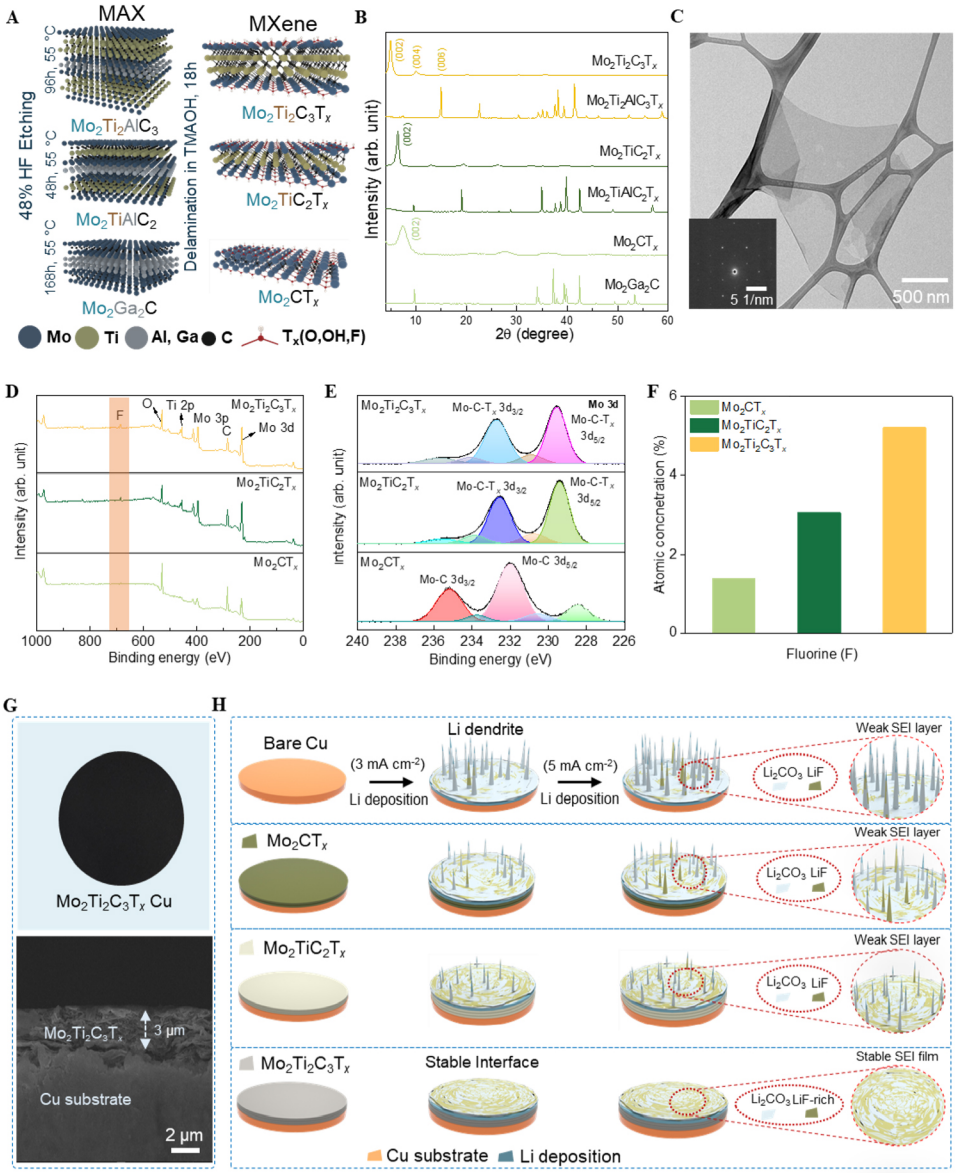

Figure 1. (A) Schematics of the synthesis of the $Mo_2Ti_2C_3T_x$, $Mo_2TiC_2T_x$, and Mo_2CT_x MXenes. (B) XRD patterns of the $Mo_2Ti_2C_3T_x$, $Mo_2TiC_2T_x$, and Mo_2CT_x MXenes and their corresponding MAX phases (Mo_2Ga_2C, Mo_2TiAlC_2, and $Mo_2Ti_2AlC_3$). (C) TEM single-flake image and SAED pattern of the $Mo_2Ti_2C_3T_x$. (D) XPS survey spectrum of the $Mo_2Ti_2C_3T_x$, $Mo_2TiC_2T_x$, and Mo_2CT_x MXenes. (E) deconvoluted Mo 3d spectra of the $Mo_2Ti_2C_3T_x$, $Mo_2TiC_2T_x$, and Mo_2CT_x. (F) Composition comparison of fluorine termination on the $Mo_2Ti_2C_3T_x$, $Mo_2TiC_2T_x$, and Mo_2CT_x. (G) Digital photograph and cross-sectional SEM image of the $Mo_2Ti_2C_3T_x$ electrode coated on Cu substrate. (H) Schematics of the fabrication of the $Mo_2Ti_2C_3T_x$, $Mo_2TiC_2T_x$, Mo_2CT_x, and bare Cu electrodes, and the effect of the electrode on the Li deposition at different current densities, with emphasis on the *in-situ* formation of a Li_2CO_3/LiF-rich SEI layer on the electrode.

Half-cell battery performance with different electrodes

To investigate the electrochemical performance of the $Mo_2Ti_2C_3T_x$, $Mo_2TiC_2T_x$, Mo_2CT_x, and bare Cu electrodes, asymmetric half-cells were assembled using lithium metal foil to serve as the counter/reference electrode. PP separator (Celgard 3501) was used, and the electrolyte consisted of 1M LiTFSI in a mixture of DOL and DME with 5 wt.% $LiNO_3$. Galvanostatic lithium metal deposition tests were conducted at a fixed cut-off capacity of 0.5 mAh·cm^{-2} with an areal current density of 50 uA cm^{-2} [Figure 2A]. The $Mo_2Ti_2C_3T_x$||Li electrode exhibited a reduced overpotential of 13 mV, compared to the overpotentials of the $Mo_2TiC_2T_x$||Li,

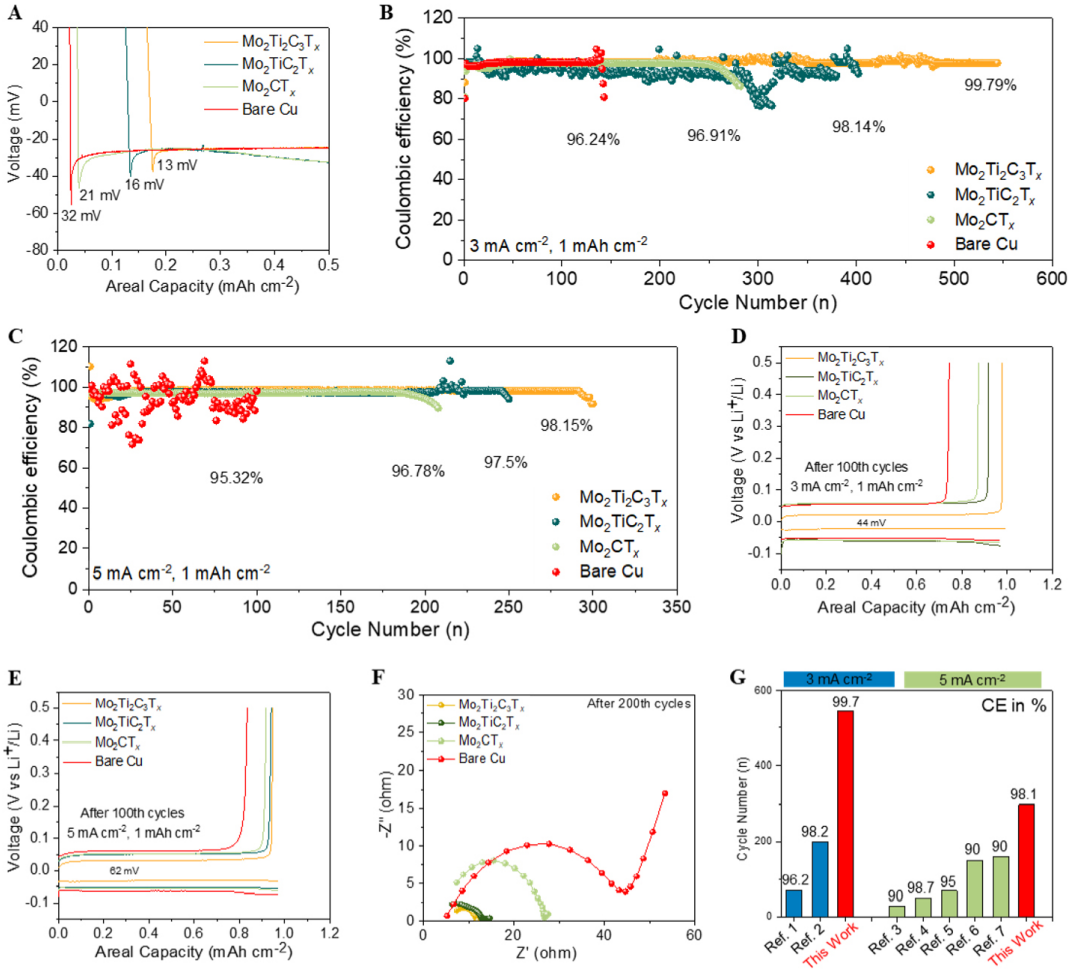

Figure 2. Half-cell performance test. (A) Nucleation overpotential at current density of 0.05 mA cm^{-2} with fixed capacity of 0.5 mAh cm^{-2}. (B) Cycling stability at current density of 3 mA cm^{-2} and areal capacity of 1 mAh cm^{-2}. (C) Cycling stability at current density of 5 mA cm^{-2} and areal capacity of 1 mAh cm^{-2}. (D) Voltage profiles of plating/stripping after 100 cycles at current density of 3 mA cm^{-2} and fixed capacity of 1 mAh cm^{-2}. (E) Voltage profiles of plating/stripping after 100 cycles at current density of 5 mA cm^{-2} and fixed capacity of 1 mAh cm^{-2}. (F) EIS analysis after 200 cycles at 3 mA cm^{-2} with fixed capacity of 1 mAh cm^{-2}. (G) Comparison of the half-cell performance of the $Mo_2Ti_2C_3T_x$ electrode with the previous literature.

Mo_2CT_x||Li, and bare Cu||Li electrodes of ~16, 21, and 32 mV, respectively, indicating the lowest energy barrier for Li nucleation on the $Mo_2Ti_2C_3T_x$ surface, compared to the other substrates. The overpotential for all the substrates increased with the current density due to ohmic polarization [Supplementary Figure 9]. Notably, the $Mo_2Ti_2C_3T_x$||Li cell exhibited the lowest hysteresis values among the MXenes at 25, 44.32, 56.3, 78.21, and 125.03 mV for current rates of 0.2, 0.5, 1, 3, and 5 mA cm^{-2}, respectively. This performance surpasses that of the $Mo_2TiC_2T_x$||Li, Mo_2CT_x||Li, and bare Cu||Li electrodes. To investigate the long-term cycling performance of asymmetric cells, we evaluated the $Mo_2Ti_2C_3T_x$||Li, $Mo_2TiC_2T_x$||Li, Mo_2CT_x||Li, and bare Cu||Li at fixed capacity of 1 mAh cm^{-2} with high current densities of 3 and 5 mA cm^{-2} [Figure 2B and C]. At current density of 3 mA cm^{-2} with fixed capacity of 1 mAh cm^{-2} [Figure 2B], the $Mo_2Ti_2C_3T_x$ substrate exhibited a superior CE of 99.79% over 544 cycles, significantly surpassing that of the $Mo_2TiC_2T_x$ (98.14%, 402), Mo_2CT_x (96.91%, 282), and bare Cu (96.24%, 143). This advantage is maintained at a much higher current density of 5 mA cm^{-2}, where the $Mo_2Ti_2C_3T_x$ cell maintains a CE above 98% for 298 cycles, while the $Mo_2TiC_2T_x$, Mo_2CT_x, and bare Cu electrodes quickly short [Figure 2C]. Furthermore, when we evaluated the voltage profiles of the $Mo_2Ti_2C_3T_x$, $Mo_2TiC_2T_x$, Mo_2CT_x, and bare Cu electrode cells, after

100 cycles at current densities of 3 and 5 mA cm^{-2}, the $Mo_2Ti_2C_3T_x$ electrode demonstrated significantly lower hysteresis and high-capacity retention, as compared to the other substrates [Figure 2D and E].

In the EIS measurements, the cell with the $Mo_2Ti_2C_3T_x$ electrode exhibited reduced impedance of 11.5 Ω after 200 cycles, compared to the 13, 26, and 44 Ω for the $Mo_2TiC_2T_x$, Mo_2CT_x, and bare Cu electrodes, respectively [Figure 2F]. These experimental results confirm that the Mo-based MXenes substrate facilitates lithium deposition, leading to low overpotential behavior, and superior CE, capacity retention, and cycling performance, compared to the Cu substrate. Among them, the $Mo_2Ti_2C_3T_x$ exhibited the lowest overpotential, the highest Coulombic efficiency, and the most prolonged cycling stability, which surpassed those of all the previously reported studies, including LASS-Cu[30], Cu-Ag[31], Nitrogen-carbon Cu nanorod[32], 3D porous copper[33], ZnO-Cu Zn mesh[34], PNIPAM polymer Cu[35], and $Ti_3C_2T_x$ Cu[36] [Figure 2G and Supplementary Table 2]. This performance also surpasses our previous findings on $Ti_3C_2T_x$ MXenes with -F termination[19], which demonstrated cycling stability over 300 cycles in an asymmetric cell at a current density of 2 mA cm^{-2}. In this current study, the $Mo_2Ti_2C_3T_x$ anode exhibits even longer cycling stability at a higher current rate (544 cycles at 3 mA cm^{-2}). We attribute this enhanced stability to the synergistic effect of the Mo-Ti bimetallic composition, coupled with the higher density of -F terminations, which results in superior cycling performance at higher current rates compared to the single-metallic $Ti_3C_2T_x$ MXenes.

Furthermore, in terms of polymer coatings, a study by Wang *et al.* demonstrated the use of polyethylene oxide (PEO) for SEI stabilization, achieving stability over 75 cycles at a current density of 5 mA cm^{-2} with a CE of 94.8%[37]. In another study, Fei *et al.* explored the use of the natural biopolymer guar gum (GG) as an artificial SEI layer, though this configuration was stable for only 100 cycles at current density of 2 mA cm^{-2}[38]. A more recent report investigated fluorosulfonyl fluoropolymers as an artificial SEI layer[39], demonstrating stability for 200 cycles with a CE of 98.6% at a current density of 1 mA cm^{-2}.

When comparing with alloy anodes, the Li-Ge alloy has been used to form a hybrid SEI layer[40], achieving 300 cycles with a CE of 98.5%. Similarly, a lithiophilic alloy film composed of ZnMgTiAl[41] deposited on Cu foil exhibited a CE of 89.5% after 200 cycles at a current density of 2 mA cm^{-2}. These comparisons highlight that the Mo-based MXenes, particularly $Mo_2Ti_2C_3T_x$, outperformed several other SEI stabilization systems, including polymer coating and alloy anodes. $Mo_2Ti_2C_3T_x$ exhibits long cycling stability of 544 and 298 cycles with high CE, particularly at high current densities of 3 and 5 mA cm^{-2}, underscoring its superior performance.

Morphology of Li deposition on different substrates

To investigate the Li deposition behavior on the MXene electrodes, SEM analysis was performed on the electrode surfaces after 200 cycles at areal capacity of 1 mAh cm^{-2} and current densities of 3 and 5 mA cm^{-2} [Figure 3]. The bare Cu electrode, used as a control, exhibited sharp lithium dendritic growth on the surface at 3 mA cm^{-2} [Figure 3B], which became even more pronounced at the higher current density of 5 mA cm^{-2} [Figure 3C]. This indicates that the Cu electrode leads to uncontrolled and irregular lithium deposition on the surface, resulting in significant dendrite formation. The Mo_2CT_x electrode displayed severe non-uniform lithium growth on the surface, similar to the bare Cu electrode [Figure 3E and F], indicating strong dendritic growth behavior. The dendritic growth of lithium on the bare Cu and monometallic Mo_2CT_x electrodes can be attributed to the high nucleation potential barriers, which cause Li to preferentially deposit on the existing lithium metal, rather than directly on the electrode surface. This leads to severe dendritic growth and uneven Li deposition, particularly at higher current densities, ultimately degrading the Coulombic efficiency and cycling stability.

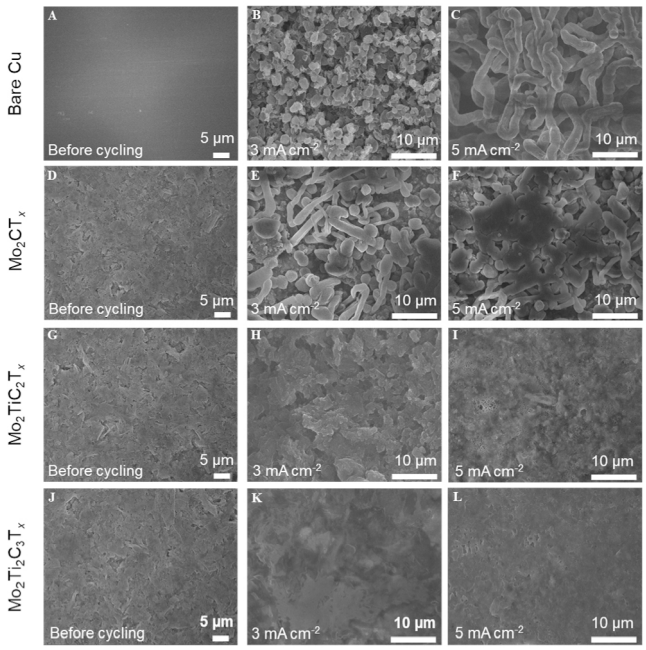

Figure 3. Top view SEM images of Li deposited on the $Mo_2Ti_2C_3T_x$, $Mo_2TiC_2T_x$, Mo_2CT_x, and bare Cu electrodes after 200 cycles at 3 and 5 mA cm^{-2} with fixed capacity of 1 mAh cm^{-2}. (A-C) The bare Cu, (D-F) Mo_2CT_x, (G-I) $Mo_2TiC_2T_x$, and (J-L) $Mo_2Ti_2C_3T_x$.

Surprisingly, the bimetallic $Mo_2TiC_2T_x$ and $Mo_2Ti_2C_3T_x$ MXenes exhibited significant changes in surface morphology. The $Mo_2TiC_2T_x$ electrode showed much smoother surface morphology, compared to the Cu and Mo_2CT_x electrodes [Figure 3H and I]. However, small dendrites were still present on the surface at current densities of 3 and 5 mA cm^{-2}, indicating that while the bimetallic $Mo_2TiC_2T_x$ offers some improvement over the Mo_2CT_x, it is still insufficient to completely prevent dendrite formation, especially at higher current density of 5 mA cm^{-2}. In contrast, the $Mo_2Ti_2C_3T_x$ electrode demonstrated a more homogeneous and uniform surface morphology [Figure 3K and L]. At a current density of 3 mA cm^{-2}, the Li deposition remained uniform, and free of significant dendritic structures [Figure 3K]. Even at the higher current density of 5 mA cm^{-2}, the $Mo_2Ti_2C_3T_x$ electrode continued to exhibit a smooth and uniform surface [Figure 3L], indicating superior control over Li deposition, compared to the other electrodes. Consequently, the bimetallic $Mo_2Ti_2C_3T_x$ substrate, characterized by the lowest Li nucleation energy barrier, achieved the most uniform lithium deposition, and effectively suppressed dendritic growth, which is attributed to its excellent Coulombic efficiency and extended cycling stability.

Characterization of the solid electrolyte interphase layers

To examine the atomic characteristic of the solid electrolyte interphase (SEI) layers on the $Mo_2Ti_2C_3T_x$, $Mo_2TiC_2T_x$, Mo_2CT_x, and bare Cu electrodes, XPS survey-scan analysis was conducted on the electrode surfaces after three charge-discharge cycles at a current density of 1 mA cm^{-2} with an areal capacity of 1 mAh cm^{-2} [Figure 4A and B]. The XPS survey spectra [Figure 4A] confirmed the presence of Li, C, O, and F atoms in the SEI layer across all samples. Detailed atomic composition analysis revealed that the composition of the SEI layer varies significantly, depending on the type of electrode [Figure 4B]. On moving from the $Mo_2Ti_2C_3T_x$ to the $Mo_2TiC_2T_x$, Mo_2CT_x, and bare Cu electrodes, the Li and F content gradually decreases, while the C content increases. Notable, a key distinction among the SEIs is the higher F content in the $Mo_2Ti_2C_3T_x$ electrode, reaching 35%, compared to 28%, 24% and 17% in the $Mo_2TiC_2T_x$, Mo_2CT_x, and bare Cu electrodes, respectively. Another significant difference is the lower C content (12%) in the $Mo_2Ti_2C_3T_x$ electrode, compared to the 20%, 23% and 34% in the $Mo_2TiC_2T_x$, Mo_2CT_x, and bare Cu

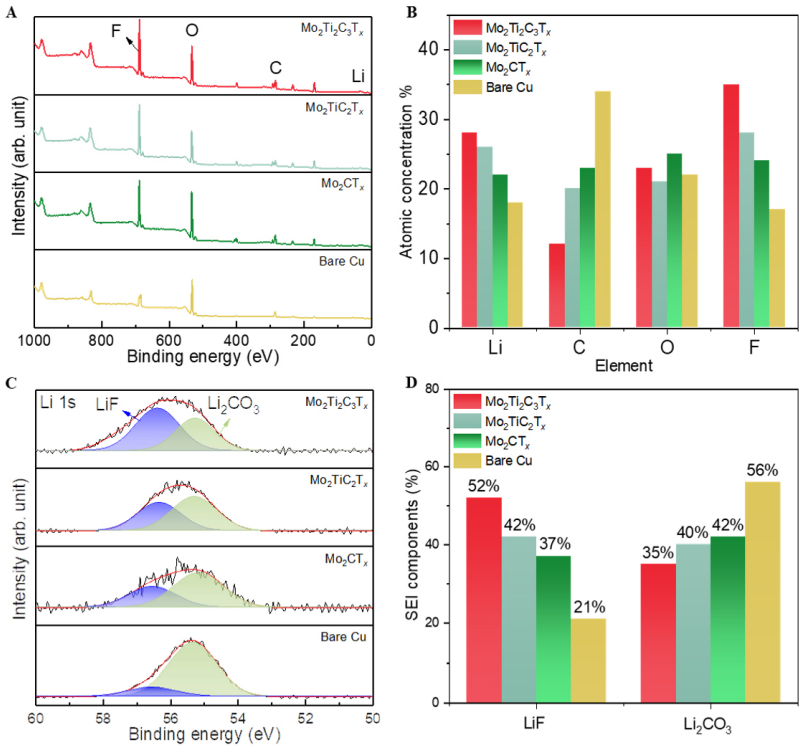

Figure 4. XPS analysis of the SEI layer. (A) XPS survey spectra of the $Mo_2Ti_2C_3T_x$, $Mo_2TiC_2T_x$, Mo_2CT_x, and the bare Cu. (B) Atomic concentration of Li, F, C, and O in the SEI layer. (C) Li 1s XPS spectra. (D) Relative percentage of different components in the SEI layer of the $Mo_2Ti_2C_3T_x$, $Mo_2TiC_2T_x$, Mo_2CT_x, and bare Cu electrodes.

substrates, respectively. The Li 1s spectra provide further structural insight into the SEI layers [Figure 4C], with all four electrodes exhibiting two characteristic peaks nearly at about 56.4 and 55.3 eV, corresponding to LiF and Li_2CO_3, respectively[42-44]. Quantitative analysis of the LiF and Li_2CO_3 in the SEI layers [Figure 4D] revealed that the $Mo_2Ti_2C_3T_x$ SEI contains a higher proportion of inorganic LiF component, approximately 52%, compared to 42% in the $Mo_2TiC_2T_x$, 37% in the Mo_2CT_x, and 21% in the bare Cu.

The increased LiF content in the $Mo_2Ti_2C_3T_x$, $Mo_2TiC_2T_x$, and Mo_2CT_x, compared to the Cu electrode, can be attributed to the F-terminations on the surface of MXenes, which result from the etching synthesis process, as shown in Figure 1F. The $Mo_2Ti_2C_3T_x$ SEI layer, being the richest in LiF, is likely due to the higher concentration of F-terminations on the surface of the $Mo_2Ti_2C_3T_x$ MXene. Conversely, the Li_2CO_3 component is relatively low in the $Mo_2Ti_2C_3T_x$ SEI, at 35%, compared to the 40%, 42% and 56% in the $Mo_2TiC_2T_x$, Mo_2CT_x, and bare Cu SEIs, respectively. Note that the remaining SEI composition is primarily organic, mainly consisting of $-CF_3$ species originating from the intermediate reduction products of the anions such as bis(trifluoromethanesulfonyl)imide ($TFSI^-$)[45,46].

This variation in the chemical composition of the SEI layers significantly influences the electrochemical performance of the $Mo_2Ti_2C_3T_x$, $Mo_2TiC_2T_x$, Mo_2CT_x, and bare Cu electrodes, as illustrated in Figure 1H. In this study, LiF and Li_2CO_3 inorganic SEI components were formed on the anode electrodes during charge-discharge cycles. LiF, known for its high ionic conductivity, excellent chemical stability, and robust mechanical strength, is effective at suppressing lithium dendrite growth and enhancing cycling stability[47,48]. Additionally, the inorganic LiF crystals exhibit a wide band gap and a low lithium-ion diffusion barrier, which are crucial for promoting uniform lithium deposition and preventing lithium dendrite formation.

Several studies have demonstrated that a LiF-rich SEI layer plays a key role in ensuring homogeneous Li-ion deposition[8]. The high ionic conductivity allows Li^+ ions to diffuse through the LiF layer with minimal resistance, while the low diffusion barrier facilitates smooth ion transport across the SEI. This ensures uniform lithium deposition on the electrode surface, effectively minimizing the risk of dendrite formation.

Furthermore, the lithiophilic nature of LiF lowers the energy required for lithium nucleation, reducing nucleation overpotential during the deposition process. This low diffusion energy promotes an even distribution of Li^+ ions across the electrode, preventing concentration gradients that typically lead to dendritic growth. By lowering both the diffusion and nucleation energy barriers, LiF ensures a uniform lithium deposition, resulting in a smooth layer instead of sharp dendritic structures. Therefore, the LiF-rich SEI layer plays a crucial role in stabilizing lithium deposition and preventing dendrite formation, significantly enhancing the overall performance of the electrode.

In contrast, Li_2CO_3, with lower ionic conductivity and stability, is less effective at preventing dendrite formation, and is more prone to degradation, which can limit long-term battery performance[49,50]. Li_2CO_3 can have both beneficial and detrimental effects on the battery cycling performance depending on its concentration. In small amounts, Li_2CO_3 assists in the initial SEI formation by providing a protective layer. However, an excess of Li_2CO_3 is typically detrimental as it increases resistivity, reduces chemical stability, and accelerates SEI degradation. This leads to higher impedance and reduced cycling performance[49].

A LiF-dominant SEI is more favorable for long-term cycling stability due to its lower impedance, ability to promote uniform lithium deposition, and suppression of dendrite formation. In contrast, a Li_2CO_3-rich SEI is often linked to higher impedance and faster capacity fade, making it less suitable for sustained cycling. Therefore, maintaining a high LiF-to-Li_2CO_3 ratio in the SEI is essential for enhancing long-term electrochemical performance.

Consequently, from the chemical perspective, the bimetallic $Mo_2Ti_2C_3T_x$ MXenes exhibit a higher density of fluorine terminations on the surface compared to other Mo-based MXenes, such as Mo_2CT_x and $Mo_2TiC_2T_x$. These -F rich terminations facilitate the formation of a stable LiF-rich SEI layer, which enables faster Li-ion transport through the SEI, more efficient and uniform lithium nucleation and deposition without dendrite formation, and ultimately, excellent Coulombic efficiency and prolonged cycling performance[51,52].

Additionally, from an electronic standpoint, the inclusion of Ti in the Mo-based MXene structure enhances its electronic properties by creating additional energy states near the Fermi level, improving electronic conductivity. This is critical for efficient Li-ion transport and deposition in LMBs. Compared to Mo_2CT_x and $Mo_2TiC_2T_x$, the presence of an additional Ti layer in $Mo_2Ti_2C_3T_x$ modifies the electronic structure, increasing both the electron density and the density of states (DOS). This leads to improved charge transfer kinetics during battery cycling[53,54]. Furthermore, the bimetallic $Mo_2Ti_2C_3T_x$ offers a more interconnected lattice structure than other Mo-based MXenes, which enhances Li-ion diffusion pathways and reduces the energy barrier for Li-ion transport[55]. Therefore, the bimetallic Mo-Ti composition in the $Mo_2Ti_2C_3T_x$ plays a crucial role in stabilizing the SEI layer and enhancing battery performance through both chemical and electronic mechanisms.

Full-cell battery performance

The full cell performance of the $Mo_2Ti_2C_3T_x$, $Mo_2TiC_2T_x$, Mo_2CT_x, and bare Cu anodes, paired with an NCM622 cathode that has a high cathode loading of 10 mg cm^{-2}, was evaluated. The cells, designated as Li/$Mo_2Ti_2C_3T_x$||NCM622, Li/$Mo_2TiC_2T_x$||NCM622, Li/Mo_2CT_x||NCM622, and Li/Cu||NCM622,

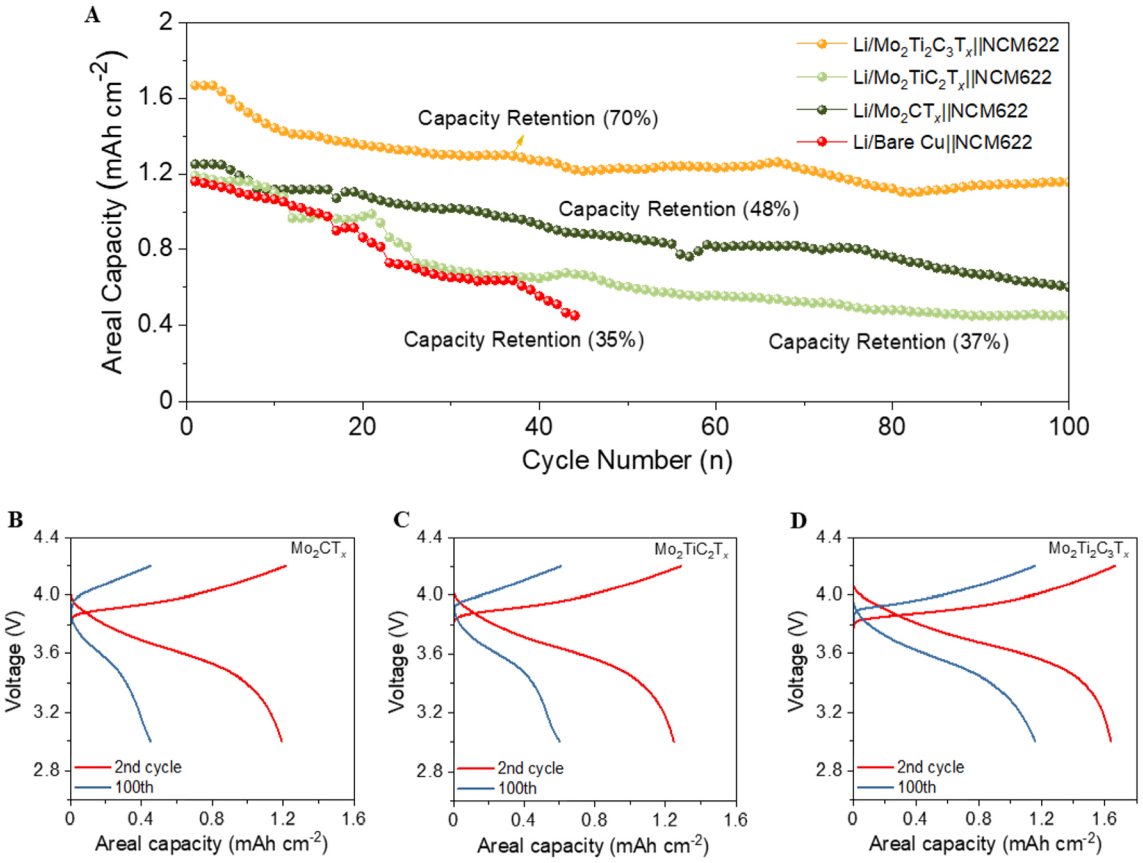

Figure 5. Full cell performance comparison (A) Cycling performances comparison of the Li/$Mo_2Ti_2C_3T_x$||NCM622, Li/$Mo_2TiC_2T_x$||NCM622, Li/Mo_2CT_x||NCM622, and Li/Cu||NCM622 at 0.5 C. Voltage profiles of the 2nd and 100th cycle of the (B) Li/Mo_2CT_x||NCM622, (C) Li/$Mo_2TiC_2T_x$||NCM622, and (D) Li/$Mo_2Ti_2C_3T_x$||NCM622.

respectively, were evaluated at 0.5 C rate within a voltage window of 3.0 to 4.2 V [Figure 5A]. The anodes were pre-deposited with Li of 3 mAh cm^{-2} capacity before cycling as shown in Supplementary Figure 10, and the electrolyte used was 1 M $LiPF_6$ in EC/DMC (1/1, v/v). The Li/$Mo_2Ti_2C_3T_x$||NCM622 full cell demonstrated stable cycling for 100 cycles, before its capacity dropped to 70%. In contrast, the capacities of the Li/$Mo_2TiC_2T_x$||NCM622, Li/Mo_2CT_x||NCM622, and Li/Cu||NCM622 cells fell to 48%, 37% and 35%, respectively, highlighting the superiority of the $Mo_2Ti_2C_3T_x$ electrode. Additionally, in the initial cycle, the Li/$Mo_2Ti_2C_3T_x$||NCM622 cell exhibited a higher discharge capacity (1.64 mAh cm^{-2}), compared to the Li/$Mo_2TiC_2T_x$||NCM622, Li/Mo_2CT_x||NCM622, and Li/Cu||NCM622 at 1.24, 1.19, and 1.16 mAh cm^{-2}, respectively. After 100 cycles, the capacity of the Li/$Mo_2Ti_2C_3T_x$||NCM622 cell remained at 1.16 mAh cm^{-2}, while the capacities of the Li/$Mo_2TiC_2T_x$||NCM622, Li/Mo_2CT_x||NCM622, and Li/Cu||NCM622 cells had decreased to 0.60, 0.45, and 0.43 mAh cm^{-2}, respectively [Figure 5B-D]. The voltage profiles of the Li/Cu||NCM622 are provided in Supplementary Figure 11. The energy densities of the full cells are 530.6, 405.1, 387.2, and 380.0 Wh/kg for $Mo_2Ti_2C_3T_x$, $Mo_2TiC_2T_x$, Mo_2CT_x, and Bare Cu anodes, respectively. The comprehensive comparison table outlining the performance of all MXenes, along with the bare Cu reference sample in this study, can be found in [Supplementary Table 3]. Our results are consistent with the previously reported studies [Supplementary Table 4] and demonstrate significantly enhanced performance, attributed to the formation of a more stable LiF-rich/Li_2CO_3 SEI layer induced by the surface chemistry of the $Mo_2Ti_2C_3T_x$ substrate. The excellent cycling stability and high capacity in carbonate-based electrolytes underscore the great potential of $Mo_2Ti_2C_3T_x$ anode substrates for practical Li-metal batteries.

CONCLUSION

Three different Mo-based MXenes - Mo_2CT_x, $Mo_2TiC_2T_x$, and $Mo_2Ti_2C_3T_x$ - were synthesized and evaluated for their electrochemical performances as an anode for LMBs. The surface chemistry of these Mo-based MXenes plays a critical role in the formation of the SEI layer. Among them, the bimetallic $Mo_2Ti_2C_3T_x$ exhibited the most stable LiF-rich SEI layer, which is attributed to its abundant F surface terminations. This stabilization of the SEI layer enhances Li-ion transport, enables uniform lithium nucleation and deposition without dendrite growth, and ultimately results in excellent Coulombic efficiency and prolonged cycling performance. Consequently, the $Mo_2Ti_2C_3T_x$ achieved extended cycling stability of 544 cycles with Coulombic efficiency of 99.79% at high current density of 3 mA cm^{-2} and capacity of 1 mAh cm^{-2}. In full cells, the $Mo_2Ti_2C_3T_x$ anode, paired with an NCM622 cathode, maintained 70% capacity retention over 100 cycles with high cathode loading of 10 mg cm^{-2}. This study underscores the promising potential of Molybdenum-based MXenes as anode materials for the next-generation high-energy-density LMBs.

DECLARATIONS

Author's contribution

Designed the experiment, performed the physical characterization, electrochemical measurements, and data analysis, and wrote the manuscript: Zaman, S.
Performed the physical characterization, and revised the manuscript: Narayanasamy, M.
Designed the schematics, and revised the manuscript: Naqvi, S. M.
Performed experiments, and revised the manuscript: Hassan, T.
Revised the manuscript: Iqbal, A.; Hussain, N.; Cho, S. Y.; Jung, S.
Performed the SEM measurements, and revised the manuscript: Zafar, U.
Assisted with the XPS analysis: Jeong, S.
Conceptualized and coordinated the activities, provided funding for the work, and revised the manuscript: Koo, C. M.

Availability of data and materials

All the data supporting the findings of this study are available within the article and its ESI. Additional data related to this article can be obtained from the corresponding author upon reasonable request.

Financial support and sponsorship

This study was supported by grants from the Basic Science Research Program (2021M3H4A1A03047327 and 2022R1A2C3006227) through the National Research Foundation of Korea, funded by the Ministry of Science, ICT, and Future Planning; the Fundamental R&D Program for Core Technology of Materials and the Industrial Strategic Technology Development Program (20020855), funded by the Ministry of Trade, Industry, and Energy, Republic of Korea; and the National Research Council of Science & Technology (NST), funded by the Korean Government (MSIT) (CRC22031-000). Furthermore, this research was partially supported by the Ministry of Trade, Industry and Energy(MOTIE), Korea Institute for Advancement of Technology(KIAT) through the International Cooperative R&D program (P0028332).

Conflicts of interest

All authors declared that there are no conflicts of interest.

Ethical approval and consent to participate

Not applicable.

Consent for publication

Not applicable.

REFERENCES

1. Jiao, S.; Zheng, J.; Li, Q.; et al. Behavior of lithium metal anodes under various capacity utilization and high current density in lithium metal batteries. *Joule* **2018**, *2*, 110-24. DOI
2. Li, G.; Liu, Z.; Huang, Q.; et al. Stable metal battery anodes enabled by polyethylenimine sponge hosts by way of electrokinetic effects. *Nat. Energy.* **2018**, *3*, 1076-83. DOI
3. Zhao, L.; Ding, B.; Qin, X. Y.; et al. Revisiting the roles of natural graphite in ongoing lithium-ion batteries. *Adv. Mater.* **2022**, *34*, e2106704. DOI
4. Kim, J. M.; Engelhard, M. H.; Lu, B.; et al. High current-density-charging lithium metal batteries enabled by double-layer protected lithium metal anode. *Adv. Funct. Mater.* **2022**, *32*, 2207172. DOI
5. Wang, T.; Li, Y.; Zhang, J.; et al. Immunizing lithium metal anodes against dendrite growth using protein molecules to achieve high energy batteries. *Nat. Commun.* **2020**, *11*, 5429. DOI PubMed PMC
6. Lin, D.; Liu, Y.; Cui, Y. Reviving the lithium metal anode for high-energy batteries. *Nat. Nanotechnol.* **2017**, *12*, 194-206. DOI PubMed
7. Cheng, X. B.; Zhang, R.; Zhao, C. Z.; Zhang, Q. Toward safe lithium metal anode in rechargeable batteries: a review. *Chem. Rev.* **2017**, *117*, 10403-73. DOI PubMed
8. Tan, J.; Matz, J.; Dong, P.; Shen, J.; Ye, M. A growing appreciation for the role of LiF in the solid electrolyte interphase. *Adv. Energy. Mater.* **2021**, *11*, 2100046. DOI
9. von Aspern N, Röschenthaler GV, Winter M, Cekic-Laskovic I. Fluorine and lithium: ideal partners for high-performance rechargeable battery electrolytes. *Angew. Chem. Int. Ed.* **2019**, *58*, 15978-6000. DOI PubMed
10. Alvarado, J.; Schroeder, M. A.; Pollard, T. P.; et al. Bisalt ether electrolytes: a pathway towards lithium metal batteries with Ni-rich cathodes. *Energy. Environ. Sci.* **2019**, *12*, 780-94. DOI
11. Weber, R.; Genovese, M.; Louli, A. J.; et al. Long cycle life and dendrite-free lithium morphology in anode-free lithium pouch cells enabled by a dual-salt liquid electrolyte. *Nat. Energy.* **2019**, *4*, 683-9. DOI
12. Umh, H. N.; Park, J.; Yeo, J.; Jung, S.; Nam, I.; Yi, J. Lithium metal anode on a copper dendritic superstructure. *Electrochem. Commun.* **2019**, *99*, 27-31. DOI
13. Yan, K.; Lu, Z.; Lee, H. W.; et al. Selective deposition and stable encapsulation of lithium through heterogeneous seeded growth. *Nat. Energy.* **2016**, *1*, 16010. DOI
14. Jiang, G.; Li, F.; Wang, H.; et al. Perspective on high-concentration electrolytes for lithium metal batteries. *Small. Struct.* **2021**, *2*, 2000122. DOI
15. Chae, S. U.; Yi, S.; Yoon, J.; et al. Highly defective Ti_3CNT_x-MXene-based fiber membrane anode for lithium metal batteries. *Energy. Storage. Mater.* **2022**, *52*, 76-84. DOI
16. Lee, J. H.; Cho, Y. G.; Gu, D.; Kim, S. J. 2D $PdTe_2$ thin-film-coated current collectors for long-cycling anode-free rechargeable batteries. *ACS. Appl. Mater. Interfaces.* **2022**, *14*, 15080-9. DOI PubMed
17. Xu, M.; Zhu, Q.; Li, Y.; Gao, Y.; Sun, N.; Xu, B. Atom-dominated relay catalysis of high-entropy MXene promotes cascade polysulfide conversion for lithium-sulfur batteries. *Energy. Environ. Sci.* **2024**, *17*, 7735-48. DOI
18. Zhang, D.; Wang, S.; Li, B.; Gong, Y.; Yang, S. Horizontal growth of lithium on parallelly aligned MXene layers towards dendrite-free metallic lithium anodes. *Adv. Mater.* **2019**, *31*, e1901820. DOI
19. Ha, S.; Kim, D.; Lim, H. K.; Koo, C. M.; Kim, S. J.; Yun, Y. S. Lithiophilic MXene-guided lithium metal nucleation and growth behavior. *Adv. Funct. Mater.* **2021**, *31*, 2101261. DOI
20. Yao, W.; He, S.; Xu, J.; et al. Polypyrrole nanotube sponge host for stable lithium-metal batteries under lean electrolyte conditions. *ACS. Sustain. Chem. Eng.* **2021**, *9*, 2543-51. DOI
21. Liu, C.; Yuan, Z.; Chen, K.; et al. MXene-BN-introduced artificial SEI to inhibit dendrite growth of lithium metal batteries. *ACS. Appl. Mater. Interfaces.* **2023**, *15*, 56356-64. DOI
22. Narayanasamy, M.; Zaman, S.; Koo, C. M. 2D MXenes for all-solid-state batteries: a comprehensive review. *Mater. Today. Energy.* **2023**, *37*, 101405. DOI
23. Anasori, B.; Lukatskaya, M. R.; Gogotsi, Y. 2D metal carbides and nitrides (MXenes) for energy storage. *Nat. Rev. Mater.* **2017**, *2*, 16098. DOI
24. Anasori, B.; Xie, Y.; Beidaghi, M.; et al. Two-dimensional, ordered, double transition metals carbides (MXenes). *ACS. Nano.* **2015**, *9*, 9507-16. DOI
25. Halim, J.; Kota, S.; Lukatskaya, M. R.; et al. Synthesis and characterization of 2D molybdenum carbide (MXene). *Adv. Funct. Mater.* **2016**, *26*, 3118-27. DOI

26. Iqbal, A.; Kwon, J.; Hassan, T.; et al. Environmentally stable and highly crystalline MXenes for multispectral electromagnetic shielding up to millimeter waves. *Adv. Funct. Mater.* **2024**, 2409346. DOI
27. Iqbal, A.; Shahzad, F.; Hantanasirisakul, K.; et al. Anomalous absorption of electromagnetic waves by 2D transition metal carbonitride Ti_3CNT_x (MXene). *Science* **2020**, *369*, 446-50. DOI
28. Shahzad, F.; Alhabeb, M.; Hatter, C. B.; et al. Electromagnetic interference shielding with 2D transition metal carbides (MXenes). *Science* **2016**, *353*, 1137-40. DOI
29. Halim, J.; Cook, K. M.; Eklund, P.; Rosen, J.; Barsoum, M. W. XPS of cold pressed multilayered and freestanding delaminated 2D thin films of $Mo_2TiC_2T_z$ and $Mo_2Ti_2C_3T_z$ (MXenes). *Appl. Surf. Sci.* **2019**, *494*, 1138-47. DOI
30. Kwon, H. M.; Kim, N. H.; Hong, S. J.; et al. Uniform Li-metal growth on renewable lignin with lithiophilic functional groups derived from wood for high-performance Li-metal batteries. *Surf. Interfaces.* **2024**, *44*, 103643. DOI
31. Cui, S.; Zhai, P.; Yang, W.; et al. Large-scale modification of commercial copper foil with lithiophilic metal layer for Li metal battery. *Small* **2020**, *16*, e1905620. DOI
32. Yin, D.; Huang, G.; Wang, S.; et al. Free-standing 3D nitrogen-carbon anchored Cu nanorod arrays: *in situ* derivation from a metal-organic framework and strategy to stabilize lithium metal anodes. *J. Mater. Chem. A.* **2020**, *8*, 1425-31. DOI
33. Lin, H.; Zhang, Z.; Wang, Y.; Zhang, X. L.; Tie, Z.; Jin, Z. Template-sacrificed hot fusion construction and nanoseed modification of 3D porous copper nanoscaffold host for stable-cycling lithium metal anodes. *Adv. Funct. Mater.* **2021**, *31*, 2102735. DOI
34. Huang, S.; Zhang, W.; Ming, H.; Cao, G.; Fan, L. Z.; Zhang, H. Chemical energy release driven lithiophilic layer on 1 m^2 commercial brass mesh toward highly stable lithium metal batteries. *Nano. Lett.* **2019**, *19*, 1832-7. DOI
35. Li, N.; Ye, Q.; Zhang, K.; et al. Normalized lithium growth from the nucleation stage for dendrite-free lithium metal anodes. *Angew. Chem. Int. Ed.* **2019**, *131*, 18414-9. DOI
36. Yang, D.; Zhao, C.; Lian, R.; et al. Mechanisms of the planar growth of lithium metal enabled by the 2D lattice confinement from a $Ti_3C_2T_x$ MXene intermediate layer. *Adv. Funct. Mater.* **2021**, *31*, 2010987. DOI
37. Wang, G.; Chen, C.; Chen, Y.; et al. Self-stabilized and strongly adhesive supramolecular polymer protective layer enables ultrahigh-rate and large-capacity lithium-metal anode. *Angew. Chem. Int. Ed.* **2020**, *59*, 2055-60. DOI
38. Fei, G.; Du, Y.; Liu, X.; et al. Suppressing Li dendrite by a guar gum natural polymer film for high-performance lithium metal anodes. *J. Appl. Polym. Sci.* **2024**, *141*, e55127. DOI
39. Ma, M.; Guo, X.; Wen, P.; et al. Reactive solid polymer layer: from a single fluoropolymer to divergent fluorinated interface. *Angew. Chem. Int. Ed.* **2024**, *136*, e202407304. DOI
40. Chu, F.; Zhou, J.; Liu, J.; Tang, F.; Song, L.; Wu, F. Constructing a fluorinated interface layer enriched with Ge nanoparticles and Li-Ge alloy for stable lithium metal anodes. *Nano. Res.* **2024**, *17*, 5148-58. DOI
41. Zhang, L.; Wu, S.; Gao, J.; et al. Multi-component lithiophilic alloy film modified Cu current collector for long-life lithium metal batteries by a novel FCVA Co-deposition system. *Small* **2024**, *20*, e2402752. DOI
42. Ding, F.; Xu, W.; Chen, X.; et al. Effects of carbonate solvents and lithium salts on morphology and coulombic efficiency of lithium electrode. *J. Electrochem. Soc.* **2013**, *160*, A1894. DOI
43. Hu, X.; Li, Y.; Liu, J.; Wang, Z.; Bai, Y.; Ma, J. Constructing LiF/Li_2CO_3-rich heterostructured electrode electrolyte interphases by electrolyte additive for 4.5 V well-cycled lithium metal batteries. *Sci. Bull.* **2023**, *68*, 1295-305. DOI
44. Peng, J. Y.; Huang, J.; Li, W. J.; et al. A high-performance rechargeable Li-O_2 battery with quasi-solid-state electrolyte. *Chinese. Phys. B.* **2018**, *27*, 078201. DOI
45. Beheshti, S. H.; Javanbakht, M.; Omidvar, H.; et al. Development, retainment, and assessment of the graphite-electrolyte interphase in Li-ion batteries regarding the functionality of SEI-forming additives. *iScience* **2022**, *25*, 103862. DOI PubMed PMC
46. Zhang, B.; Ju, Z.; Xie, Q.; et al. Ti_3CNT_x MXene/rGO scaffolds directing the formation of a robust, layered SEI toward high-rate and long-cycle lithium metal batteries. *Energy. Storage. Mater.* **2023**, *58*, 322-31. DOI
47. Li, Z.; Wang, L.; Huang, X.; He, X. Unveiling the mystery of LiF within solid electrolyte interphase in lithium batteries. *Small* **2024**, *20*, e2305429. DOI
48. Zheng, J.; Ju, Z.; Zhang, B.; et al. Lithium ion diffusion mechanism on the inorganic components of the solid-electrolyte interphase. *J. Mater. Chem. A.* **2021**, *9*, 10251-9. DOI
49. Fan, L.; Zhuang, H. L.; Gao, L.; Lu, Y.; Archer, L. A. Regulating Li deposition at artificial solid electrolyte interphases. *J. Mater. Chem. A.* **2017**, *5*, 3483-92. DOI
50. Ozhabes, Y.; Gunceler, D.; Arias, T. A. Stability and surface diffusion at lithium-electrolyte interphases with connections to dendrite suppression. *arXiv* **2015**, 150405799. DOI
51. Han, B.; Zhang, Z.; Zou, Y.; et al. Poor stability of Li_2CO_3 in the solid electrolyte interphase of a lithium-metal anode revealed by cryo-electron microscopy. *Adv. Mater.* **2021**, *33*, e2100404. DOI
52. Mahne, N.; Renfrew, S. E.; McCloskey, B. D.; Freunberger, S. A. Electrochemical oxidation of lithium carbonate generates singlet oxygen. *Angew. Chem. Int. Ed.* **2018**, *57*, 5529-33. DOI PubMed PMC
53. Hussain, I.; Amara, U.; Bibi, F.; et al. Mo-based MXenes: synthesis, properties, and applications. *Adv. Colloid. Interface. Sci.* **2024**, *324*, 103077. DOI
54. Yang, Y.; Peng, J.; Shi, Z.; Zhang, P.; Arramel, A.; Li, N. Unveiling the key intermediates in electrocatalytic synthesis of urea with CO_2 and N_2 coupling reactions on double transition-metal MXenes. *J. Mater. Chem. A.* **2023**, *11*, 6428-39. DOI
55. Liu, H.; Wang, H.; Jing, Z.; Wu, K.; Cheng, Y.; Xiao, B. Bare Mo-based ordered double-transition metal MXenes as high-performance anode materials for aluminum-ion batteries. *J. Phys. Chem. C.* **2020**, *124*, 25769-74. DOI